physica status solidi b
www.pss-b.com

Multiple Avalanche Processes in Acoustic Emission Spectroscopy: Multibranching of the Energy–Amplitude Scaling

Yan Chen, Boyuan Gou, Bincheng Yuan, Xiangdong Ding, Jun Sun, and Ekhard K. H. Salje**

Several physical processes can conspire to generate avalanches in materials. Such processes include avalanche mechanisms like dislocation movements, friction processes by pinning magnetic domain walls, moving dislocation tangles, hole collapse in porous materials, collisions of ferroelectric and ferroelastic domain boundaries, kinks in interfaces, and many more. Known methods to distinguish between these species which allow the physical identification of multiavalanche processes are reviewed. A new approach where the scaling relationship between the avalanche energies E and amplitudes A is considered is then described. Avalanches with single mechanisms scale experimentally as $E = S_i A_i^2$. The energy E reflects the duration D of the avalanche and $A(t)$, the temporal amplitude. The scaling prefactor S depends explicitly on the duration of the avalanche and on details of the avalanche profiles. It is reported that S is not a universal constant but assumes different values depending on the avalanche mechanism. If avalanches coincide, they can still show multivalued scaling between E and A with different S-values for each branch. Examples for this multibranching effect in low-Ni 316L stainless steel, 316L stainless steel, polycrystalline Ni, TC21 titanium alloy, and a $Fe_{40}Mn_{40}Co_{10}Cr_{10}$ high-entropy alloy are shown.

1. Introduction

Avalanches are collective, correlated dynamical processes that are typically detected by the emission of acoustic noise. The cacophony of acoustic emission (AE) during crackling noise experiments[1–9] consists typically of sequences of acoustic signals generated by local structural changes on time scales shorter than 100 μs. The experimental lower cutoff time is ≈1 μs. Full avalanche sequences, from their onset to their duration, can span several milliseconds.[5,10] The spectrum of AE signals, as a function of time, is called, in shorthand, "AE spectra" and is often related to the appearance of avalanches of excitations in many different scenarios. Examples are the movements of phase/twin boundaries in martensites,[11–13] nucleation and growth processes during structural phase transitions,[14,15] twinning in ferroelastics,[16,17] ferroelectric domain switching,[8] dehydration processes,[18] metal–insulator transitions,[19–21] and porous collapse under stress.[22] Avalanches are so ubiquitous that one may presume that most local "jerks," namely, local abrupt movements interacting with their surroundings, give rise to avalanches. Indeed, we detect increasing numbers of avalanches in more diverse systems due to increasing sensitivity of AE detection systems, such as the Vallen system (Vallen GmbH, German).

This observation challenges the assumption that AE crackling noise in any system always reflects one single, well-defined avalanche mechanism. A further question arises whether several different jerk systems can coexist in the same sample. Systems of solitary avalanches are ideal for the investigation of classic avalanche characteristics and several analyses have been reported,[22] where no evidence was found for several interacting avalanches. In contrast, experimental observations of the simultaneous appearance of several avalanche systems (e.g., dislocations and martensitic phase transitions, twinning and metal–insulator transitions, twinning and porous collapse, etc.) are rare so far. It is the purpose of this article to show that this is not because these interactions do not happen but because the experimental methods for their observation are often insufficient.

A key purpose of avalanche research is to identify the underlying physical processes which give rise to avalanches and pattern formation. However, the universality of avalanches acts against this aim (an argument already discussed by Salje and Dahmen in ref. [5]). Focusing on the most obvious parameters, like the

Y. Chen, B. Gou, B. Yuan, X. Ding, J. Sun, E. K. H. Salje
State Key Laboratory for Mechanical Behaviour of Materials
Xi'an Jiaotong University
Xi'an 710049, China
E-mail: dingxd@mail.xjtu.edu.cn; ekhard@esc.cam.ac.UK

E. K. H. Salje
Department of Earth Sciences
University of Cambridge
Cambridge CB2 3EQ, England

The ORCID identification number(s) for the author(s) of this article can be found under https://doi.org/10.1002/pssb.202100465.

DOI: 10.1002/pssb.202100465

scaling of energy, amplitude, and duration of an avalanche, the data appear to confirm in many cases the predictions of mean field (MF) theory; they are hence nonindicative of the underlying physical processes. The fundamental question is how to identify experimental observables that let us identify the elementary processes that generate avalanches and how to enquire whether these processes are uniquely defined. Historically, a similar situation was encountered some 40 years ago in the field of the study of structural phase transitions. While some materials show phase transitions with a single-order parameter, and hence contain only one transition mechanism, most phase transitions are "complex" and involve two mechanisms or more. This observation led to the development of the field of "order parameter couplings," which enabled the breakthrough in the quantitative understanding of phase transitions and the all-important interaction between various transition mechanisms.[23,24] In this article, we argue that a similar development is required for a quantitative description of avalanches.

1.1. The Avalanche Superposition in Maximum Likelihood Analysis

Several tools have been developed toward the analysis of avalanche mixing, which we will now review in turn. The first step is to realize that avalanche spectra might contain signals of two (or more) separate avalanche systems hidden in the details of the probability distributions functions of the avalanche energy or amplitude.[25,26] Let us first focus on the analysis of the probability density $g(E)$ that accounts for the distribution of energies of avalanche events. Similar analyses can be performed for distributions of other avalanche properties. The probability density during avalanches is expected to follow a power law.

$$g(E)\mathrm{d}E = (\varepsilon - 1)(E/E_{\min})^{-\varepsilon}\mathrm{d}E/E_{\min} \tag{1}$$

where the energy exponents ε vary typically between 1.33 and 2.5.

This power law is commonly used to determine the energy exponent ε. In addition, the standard analysis is to select the data above a certain variable cutoff value E_o and to assume that the measured values correspond to random variables, independent and identically distributed according to a power law. If we fix the value of E_o, the maximum likelihood (ML) estimator for the exponent is given by[27,28]

$$1/(\varepsilon - 1) = 1/N\sum_{1}^{N}\ln\left(\frac{E_j}{E_0}\right) \tag{2}$$

where the sum extends over the N values E_j with $E_j > E_0$. In the study by Salje et al.,[25] it was then assumed that $g(E)$ contains two power-law distributions with two different exponents ε_1 and ε_2, assuming without loss of generality $\varepsilon_1 > \varepsilon_2$.

$$g(E)\mathrm{d}E = [x(\varepsilon_1 - 1)(E/E_{\min})^{-\varepsilon_1} + (1-x)(\varepsilon_2 - 1)(E/E_{\min})^{-\varepsilon_2}]\,\mathrm{d}E/E_{\min} \tag{3}$$

with $E > E_{\min}$. The fraction x of the data set relates to the first avalanche process and the fraction $(1-x)$ to the second data set. The total ML curve can then be approximated by a simple mixing fraction.

$$\varepsilon - 1 \approx \left\{x\left(\frac{E_{\min}}{E_o}\right)^{(\varepsilon_1-1)} + (1-x)\left(\frac{E_{\min}}{E_o}\right)^{(\varepsilon_2-1)}\right\} \Big/ \left\{x\left(\frac{E_{\min}}{E_o}\right)^{\varepsilon_1-1} \Big/ ((\varepsilon_1 - 1) + (1+x)\left(\frac{E_{\min}}{E_0}\right)^{(\varepsilon_2-1)/(\varepsilon_2-1)}\right\} \tag{4}$$

The ML curve increases to a maximum value with an upper bound of ε_1 and then asymptotically decays to the value ε_2. Such mixing curves have been found experimentally in complex metals,[29] mixtures of coals and sandstone,[26] creep avalanches,[30] etc. The mixing depends crucially on the ratio x between the two energy contributions.[26] If x is small, it becomes impossible to observe mixing by this method, so that the nonobservance of mixing using this method is no evidence for its absence. A typical situation is encountered when a large number of dislocations interact with the nucleation of a phase transition inside the same material. The AE signals of the dislocations contain a very large number of signals, while the nucleation generates very few, strong signals. Experimentally, the ML curves will show a predominance of dislocation movements but sparse nucleation signals that may be lost in the experimental data. The occurrence of phase transition is hence ignored, and the materials properties are misunderstood.

1.2. Duration as a Distinguishing Parameter

The second approach was first undertaken by Soto-Parra et al.[31] who discovered that avalanches in the compressed Ti−Ni shape-memory porous alloys fall into two categories. Two sequences of AE signals were observed in the same sample. The first sequence is mainly generated by detwinning at the early stages of compression, while fracture dominates the later stages near the final catastrophic failure. The energies of both sequences display power-law distributions with energy exponents $\varepsilon \simeq 2$ (twinning) and 1.7 (fracture). Nevertheless, the distinguishing feature was not the energy exponents but the scaling between the duration and energy. The two branches were clearly distinguished in the AE correlations $E(D)$ (energy versus duration plots) and shown that they correspond to two different mechanisms. Statistically, the twinning/detwinning signals display shorter durations than the fracture avalanches.

Only after distinguishing between short and long signals could the difference between the energy exponents be measured. This example illustrates the importance of the signal durations for the analysis of avalanches. Only a very small number of signals arise from fracture. Without the separation via the duration, the distinction between the two processes could not have succeeded and the identification of fracture avalanches would not have been possible.

1.3. Grouping of Avalanche Signals

Often different types of avalanches can be identified using a time sequence. For example, avalanches close to the beginning and the end of a compression experiment can have different origins. Such groups of different avalanche mechanisms were widely observed in sandstone and coal,[32,33] where avalanches show two power-law distributions with two sets of variables. At the beginning of the compression experiment, the energy exponent is 1.5, which is close to the MF value of the stress-integrated

scenario. After further compression, the exponent dropped to 1.33, which corresponds to the critical MF value.

Such groups of different avalanche mechanisms were also found in bulk metallic glasses (BMGs). For example, after the macroscopic yielding point of BMGs upon compression,[34] the released elastic energy during a slip avalanche shows two stages: a stable plastic flow stage "A" and an unstable sliding stage "B." Stage A starts from the peak load at the beginning of the first large avalanche and shows the feature that a series of small avalanches are typically followed by a large avalanche. This feature, typically, has the self-similar dynamics characterized by a power-law size distribution.[34–37] Stage B is characterized by periodically appearing large avalanches, which dominate slip dynamics and show chaotic states.[34,37]

Similar variations were documented in ferroic materials,[38] where the shifts between stress-integrated values near 1.66 and a critical value 1.33 were found together with the shift of the Hausdorff dimension of the observed domain patterns.[39] This shift is between avalanches in different topological environments and does not refer to different avalanche species. This demonstrates that the same avalanche species (like domain switching or porous collapse) can possess different energy exponents depending on the closeness to criticality. AE spectra can distinguish between these exponents and superpositions have been observed.[36]

Different avalanche species related to separate time intervals during the compression process were identified in porous Mg/Ho alloys.[29] Mg−Ho alloys are both porous and show a high density of dislocations, which slide under external tension and compression. The dislocations nucleate near sample heterogeneities. Two mechanisms compete under external forcing during structural collapse, namely, collapsing holes and the movements of dislocations. Their fingerprints for AE measurements are very different and relate to their individual signal strengths. Porous collapse generates few, very strong AE signals while dislocation movements create many but weaker AE signals. This allows the separation of the two processes even though they almost always coincide temporarily. The porous collapse follows approximately MF behavior with $\varepsilon = 1.4$. The exponent for dislocation movement is greater with $\varepsilon = 1.92$. Most importantly, the AE durations of the dislocations are circa one order of magnitude shorter than those of the porous collapse.

Similar variations were also documented in the study of slip avalanches in BMGs[40]. For each avalanche on the compressive stress−time curve, the avalanche size and duration were measured by the size and elapsed time of stress drops.[36,40,41] Two types of avalanches were classified by a crossover between small avalanches with sizes <10 MPa and large avalanches with sizes >10 MPa. Only the large avalanches are consistent with the prediction of MF theory.[40]

We now introduce a new method based on the identification of the prefactor S of the scaling $E = S_i A_i^2$ for different avalanche mechanisms.

2. Method

2.1. Sample Description

Ingot 316L stainless steel was prepared by 70–85% cold rolling with a final sheet thickness of 1.47 mm. Nickel is an austenite stabilizing element, which makes the austenite in the steel less prone to phase transformation during deformation. We denoted the ingot cold-rolled sample with a composition of 0.02C-16.4Cr-10.5Ni-1.4Mn-2.1Mo-0.5Si (wt%) as "low-Ni 316L steel," except for the sample with a higher content of nickel (12%wt).[42,43] Pure annealed Ni samples with a purity higher than 99% (wt %) were the target material.

The ingot $Fe_{40}Mn_{40}Co_{10}Cr_{10}$ high-entropy alloy, HEA, was prepared by electromagnetic levitation melting under a high-purity argon atmosphere at 1373 K for 6 h and hot forged to a 30 mm × 40 mm × 850 mm square bar, followed by water quenching.

TC21 titanium alloy with a chemical composition Ti-6Al-2Sn-2Zr-3Mo-1Cr- 2Nb-0.1Si, wt% is an α/β titanium alloy with high strength and toughness. The initial sample was forged in the β-phase region and hot-rolled into bars with a diameter of 18 mm at 940 °C. Then the bars are annealed for 4.5 h at 900 °C and cooled to room temperature in a furnace.[44]

2.2. Experimental Method

Dog-bone shaped samples with a gauge range of 25 mm × 4 mm × 1.5 mm were cut with a wire-saw. Uniaxial tensile experiments were performed on an Instron5969 Universal Testing system with a tensile rate of 0.01 mm min^{-1} at room temperature.

Electron backscatter diffraction (EBSD) measurements were conducted to characterize the evolution of the microstructure at different strains. The sample used for EBSD and its loading condition is the same as the one used for AE measurements. The deformation strains of the EBSD sample, e.g., the strain from the grip end to the fracture surface, were measured by an Instron DICREPLAY device. EBSD data were collected on a ZEISS Gemini500 field emission scanning electron microscope and evaluated by the AZtecCrystal software. X-ray diffraction (XRD) analysis were conducted on a Bruker D8 ADVANCE diffractometer. A step size of 0.01° was used for all samples. Transmission electron microscopy (TEM) was carried out on a JEOL JEM-2100Plus electron microscope with an accelerating voltage of 200 kV.

2.3. Acoustic Emission Measurements

AE signals were recorded during tensile deformation by using a piezoelectric sensor (Vallen-Systeme GmbH) with a frequency range of 200–800 kHz. The recording signals were first pre-amplified by 40 dB and then transferred for waveform analysis using an AMSY-6 AE-measurement system (Vallen-Systeme GmbH) with a sampling rate of 20 MHz. The same measurement techniques were used for other metal and alloys.

The amplitudes, durations and energies of the AE-measurement system (Vallen-Systeme GmbH) are defined as below (cf. Figure S1, Supporting Information). The Amplitudes (A) are the burst signal peak amplitude in a data set; Duration (D) is the time between the first threshold and last threshold crossing of the same signal; and Energy (E) is the integral of the squared AE-signals over time.

An AE signal is defined as a "burst" in the noise spectrum. The start of a burst is determined by a first threshold crossing and

Table 1. Properties of materials discussed in the article.

	Mechanism 1, ε	Mechanism 2, ε	$\log(S_1)$	$\log(S_2)$	S_1/S_2	Duration scale ratio
Low-Ni 316L stainless steel	Dislocation, 1.6	Martensitic transition/detwinning−twinning, 1.8	-2.66 ± 0.02	-3.33 ± 0.03	4.7 ± 0.3	5
316L stainless steel	Dislocation, 1.6	Entanglements, 1.4	-2.64 ± 0.02	-3.25 ± 0.02	4.1 ± 0.2	15
Polycrystalline Ni	Dislocation, 1.58	Detwinning, 2.0	-2.73 ± 0.03	-3.26 ± 0.03	3.3 ± 0.3	7
$Fe_{40}Mn_{40}Co_{10}Cr_{10}$ HEA	Dislocation, 1.7	Detwinning−twinning, 2.0	-2.66 ± 0.02	-3.46 ± 0.03	6.2 ± 0.5	26
TC21 titanium alloy	Dislocation slip in α-phase, 1.55	Dislocation cross in the α/β phase, Boundary and slip in another α-phase	-2.70 ± 0.01	-3.38 ± 0.01	4.8 ± 0.2	11

ended at a second threshold crossing or when the Duration Discrimination Time (DDT, defines a time period in which no threshold crossing must occur in order that an end of hit is determined) expired without any threshold crossing. A threshold of 23.3 dB was determined by prior rubber experiments to evaluate the internal noise of the experimental arrangement. The DDT is chosen as 100 µs to fit the dislocation movement (the minimum value of DDT in our instrument is 50 µs), for details of AE measurement see Ref. [43].

3. Results

3.1. Multiple $E-A^2$ Scaling in Different Alloys

We now describe the scaling of avalanches in alloys where the typical avalanche species are known to be related to dislocations, twinning, porous collapse, and nucleation events. During the experiments, we exert tension under hard boundary conditions (predescribed strain). We demonstrate the variability of S by the study of several samples that are listed in **Table 1**. The initial jerk spectra were analyzed in three different ways. First, the probability distributions for the energies are depicted as ML curves. Mixing phenomena (method 1) are observed in most spectra. The energy exponents are summarized in Table 1.

In a second step, we evaluate the scaling between the energy and the amplitudes of each material. Casals et al.[45] have already shown that the energy and amplitude of each branch of AE signals satisfies the relation $E_i = S_i A_i^2$. The change of S means a shift of two branches on a log–log scale.[45] In all materials in Table 1, we find that S is multivalued. The analysis of two branches is schematically shown in the inset of **Figure 1**. We first draw a line with slope of −0.5 in the log−log plot of $E(A)$ and then project the data points in the $E(A)$ curve to this line. The distribution of the projected points follows a double Gaussian distribution, in which each Gaussian distribution represents one branch of the AE signals. As the value of $\log(S_i)$ for each branch is the intercept of the linear fit line in the log−log plot, the uncertainty of $\log(S_i)$ can be estimated from the variation of the linear fit. The uncertainty for S_1/S_2 is estimated by the error propagation function $\delta f = \sqrt{\left(\frac{\partial f}{\partial x}\delta x\right)^2 + \left(\frac{\partial f}{\partial y}\delta y\right)^2}$, where $f(x,y) = 10^{x-y}, x = \lg(S_1), y = \lg(S_2)$, and $\delta x, \delta y, \delta f$ the uncertainty of x, y, and S_1/S_2, respectively.

The duration scale ratio is defined as the ratio of average duration of mechanism 1 and mechanism 2.

Using low-Ni 316L stainless steel as an example, we find that $S_1/S_2 = 4.7$. The ratios are summarized in Table 1; they vary between 3.3 and 6.2 with maximum relative errors less than 10%. The corresponding duration scale ratio varies between 5 and 26.

We now analyze the fine structure of the jerk profiles. The reason for $S_1/S_2 \neq 1$ is that the durations of the two avalanche species vary greatly. The information concerning the duration is contained in the energy E but not in the amplitude A_{max}. Long avalanches mean greater energies than short avalanches with the same amplitudes. After we identified the different avalanche species in the second step, we analyze the profiles for each species separately and find that avalanches of different species in Table 1 differ indeed greatly in their durations. Using low-Ni 316L stainless steel as an example, the two avalanche mechanisms were confirmed by transmission electron microscope (TEM) and electron backscatter diffraction (EBSD) to be related to dislocation movements and martensitic transformation/detwinning−twinning. Dislocation signals are longer by a factor 5 than transformation/detwinning−twinning signals.

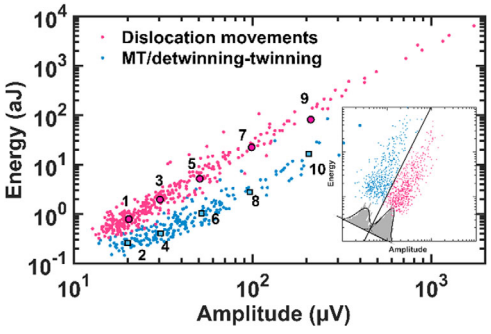

Figure 1. $E(A)$ curve of dislocation movement and martensitic transformation/detwinning−twinning with marked points for waveforms and sketch map for the separation method. The red points refer to dislocation movements and the blue points refer to martensitic transformation/detwinning−twinning. The inset in Figure 1 schematically shows how we determine the S values of the two populations in the $E-A$ correlation. AE data points of $E(A)$ for each species are projected along the direction of the $E-A$ curve in the log−log plot. They form two Gaussian distributions where their maxima define the values of S_i and their variances define the uncertainties of the determination of the S values.

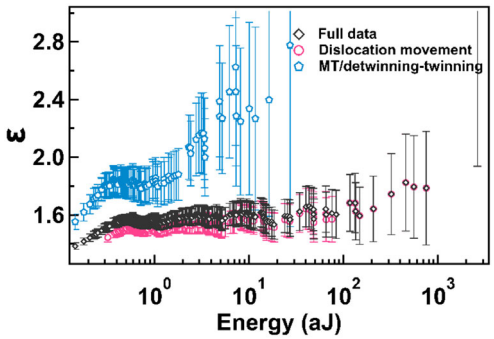

Figure 2. ML curves of dislocation movements (red), martensite transition(blue), and a full dataset (black) in low-Ni 316L stainless steel.

3.2. Avalanche Mechanisms in the Different Alloys

3.2.1. Dislocation Movement and a Mixture of Martensitic Transformation and Twinning–Detwinning in Low-Ni 316L Stainless Steel

Figure 1 summarizes two avalanche systems in low-Ni 316L stainless steel with a tensile rate of $0.01\,\mathrm{mm\,min^{-1}}$ at room temperature. The energy ratio S_1/S_2 in Figure 1 is ≈4.7, the ML curves are shown in **Figure 2**. The red curve corresponds to the movement of dislocations and the blue curve to the strain-induced nucleation of a martensitic phase together with detwinning/twinning processes. This assignment was confirmed by X-ray diffraction (XRD) (**Figure 3**a) and TEM observations (Figure 3b); see also the study by Chen et al.[42] The ML curves in Figure 2 show an energy exponent $\varepsilon = 1.5$ for dislocation movements and $\varepsilon = 1.8$ for martensitic transformation/detwinning−twinning. The combined dataset shows an energy exponent of $\varepsilon = 1.6$. Characteristic wave profiles of the AE of the same sample are shown in **Figure 4**. The time scales are hence very different for the two species with dislocation movements generating much longer AE signals than the abrupt nucleation of a martensite phase and detwinning−twinning processes. The average time ratio between the durations at the same signal amplitudes ≈ 5 (see Table 1).

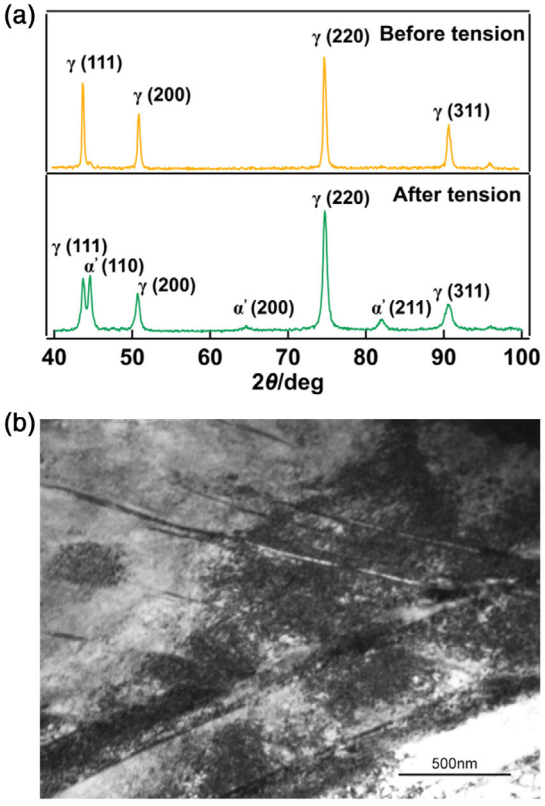

Figure 3. a) XRD diffractograms for 316L stainless steel before and after tensile experiment (tensile strain: ≈70%) show the additional martensite α' peaks. Reproduced with permission.[43] Copyright 2021, Elsevier. b) TEM image after tension (tensile strain: ≈70%) shows that martensites and dislocation microstructures coexist.

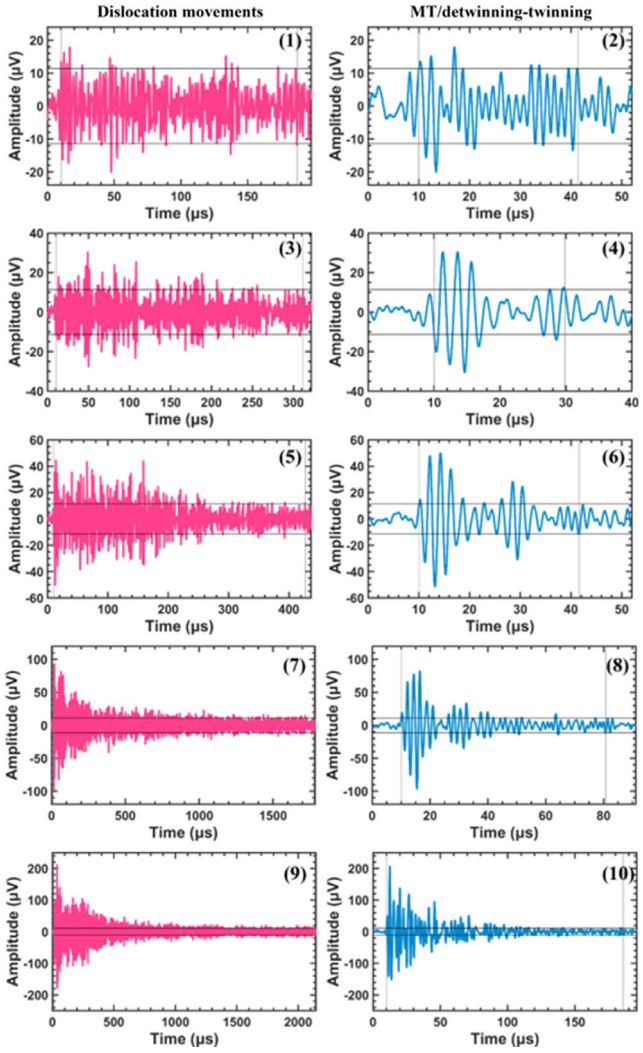

Figure 4. Examples of waveforms of dislocation movements (red) and martensitic transition/detwinning−twinning (blue) at similar amplitudes, points (1)−(10) refer to the points in Figure 1. Note the different time scales with dislocation movements extending over much longer times than martensitic transition/detwinning−twinning movements.

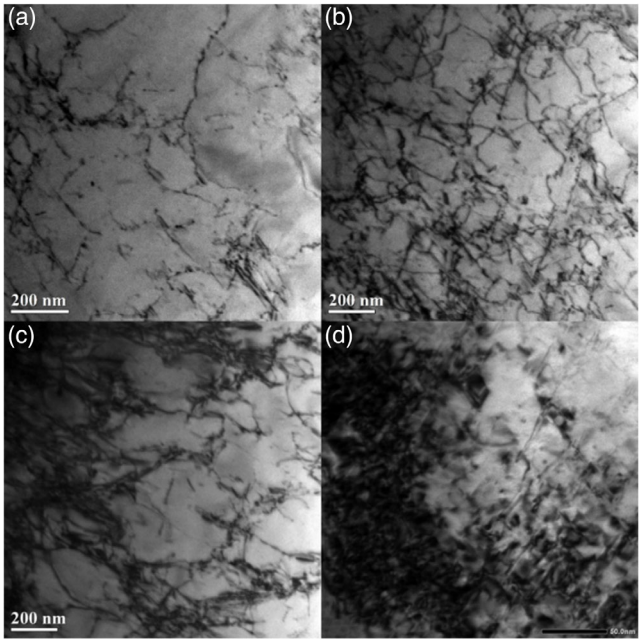

Figure 5. Dislocations in 316L stainless steel. a) Dislocations in the virgin sample, b) deformation of 1.5% with dislocation nucleation/movement, c) deformation of 13.8% with dislocation nucleation/movement and entanglement, and d) deformation after the macroscopic break point.

3.2.2. Dislocation Movement and Entanglement in 316L Stainless Steel

We now analyze dislocation movements and dynamic tangles in a typical 316L stainless steel. The dislocation motion dominates during the deformation process, while the dislocation movements were identified by TEM, as shown in **Figure 5**. The multi-branching effect is still clearly visible in **Figure 6** with two branches of the $E(A)$ scaling. The energy ratio S_1/S_2 in Figure 6 is ≈4. The ML curves in **Figure 7** confirm that the energy exponents are slightly different for the two populations and the combined spectra with ε =1.6 for dislocation movements, 1.4 for entanglements, and 1.5 for the combined data set. The duration time scales are different by a factor of 15 and the characteristic wave profiles are shown in Figure S2, Supporting Information.

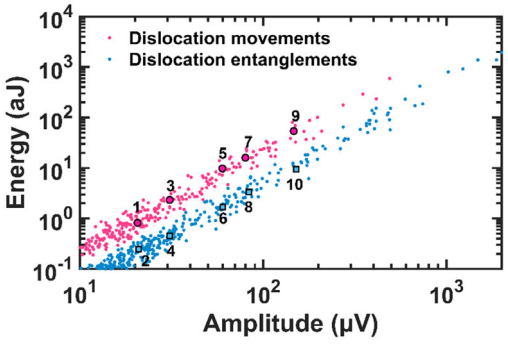

Figure 6. $E(A)$ curve of dislocation movement and entanglement with marked points for waveforms.

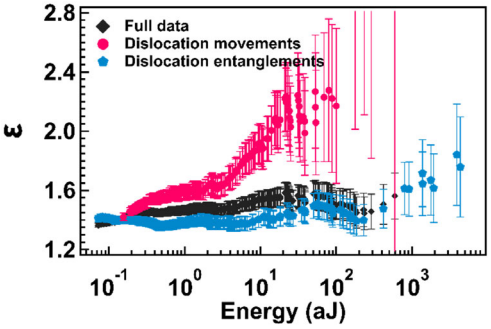

Figure 7. ML of dislocation movements (red), entanglement (blue), and full data sets in 316L steel.

3.2.3. High-Purity Polycrystalline Nickel

The grain size of annealed polycrystalline Ni (99.9% purity) is around 50 μm. Both the dislocation movement and detwinning occur during the whole deformation process. Grain rotation is also involved but only becomes observable after large plastic deformation (strain >18%, as shown in the EBSD figures of Figure S3, Supporting Information). The detwinning process before and after tension were identified by EBSD images (**Figure 8**), which indicate that the initial sample includes 38.6% growth twins, and that the twin percentage decrease to 2.47% after tension. Dislocation slip is known to be involved for pure Ni.[46,47] The deformation mechanisms in high-purity nickel shows multiple branches $E(A)$ in AE (**Figure 9**).

The energy ratio S_1/S_2 in Figure 9 is ≈3.3. For the AE signals before 18% strain, the energy exponents in **Figure 10** are very different with $\varepsilon = 1.58$ for dislocation movements, $\varepsilon = 2.0$ for detwinning dynamics, and $\varepsilon = 1.6$ for the combined data set. Although grain rotation becomes observable after large plastic deformation (strain >18%), only a few AE signals (as shown in Figure S4, Supporting Information) were detected for strain >18%. The ML analysis for the whole deformation process (Figure S5, Supporting Information) shows very similar result as that for strain <18% (Figure 10), indicating that the few AE signals from grain rotation do not change the statistics of dislocation and detwinning. The characteristic wave profiles marked in **Figure 11** are shown in Figure S6, Supporting Information.

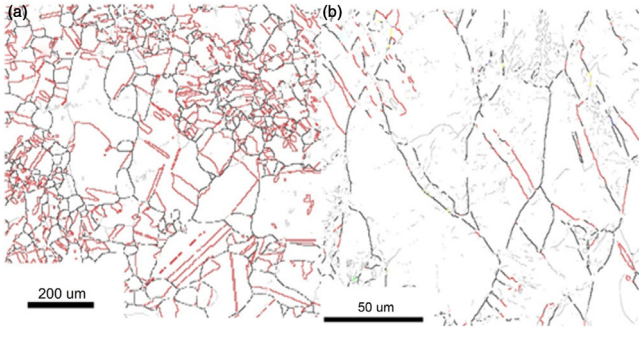

Figure 8. EBSD images of nickel a) before and b) after tension. The density of twins (marked in red) decreases from 38.6% for the virgin sample to 2.47% near the breaking point.

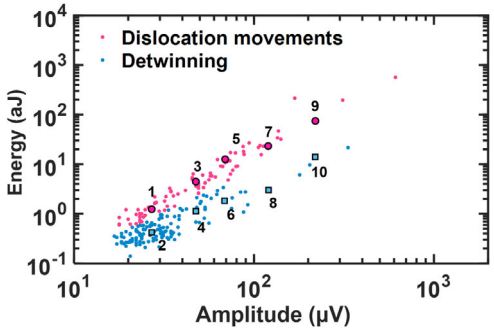

Figure 9. *E*(*A*) curve of dislocation movements (red) and detwinning (blue) in nickel with marked points for waveforms.

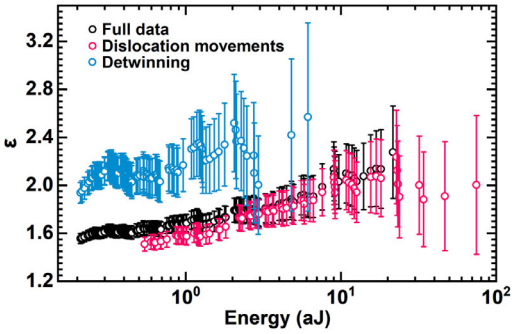

Figure 10. ML of dislocation movements (red), detwinning (blue), and full data (black) set in nickel for strain <18%.

The signal durations for dislocation and detwinning are different by a factor of 5.

3.2.4. $Fe_{40}Mn_{40}Co_{10}Cr_{10}$ High-Entropy Alloy

As seen from the EBSD results of high-entropy alloy (HEA) in Figure 11, both dislocation movement and detwinning/twinning processes occurred during deformation. The initial sample contains 57% growth twins (Figure 11a), the twins reduce to 12.7% for 40% strain (Figure 11b) and increases to 39.7% at the fracture point (Figure 11c). The "geometrically necessary dislocation" (GND) 2D maps for three different deformation states in Figure 11a-c, are shown in Figure 11d-f. The dislocation density increased during tension.

The energy ratio S_1/S_2 of two populations is ≈6.2, as shown in **Figure 12**. The population in red with an exponent $\varepsilon = 1.7$ in ML (**Figure 13**) corresponds to the dislocation movements. The other population shown by blue dots relates to detwinning/twinning process. The average durations of the two populations are different by a factor of 26, as seen from the characteristic wave profiles in Figure S7, Supporting Information.

3.2.5. TC21 Titanium Alloy with Dislocation Slips in Both α-Phase and β-Phase

The deformation mechanisms of α/β TC21 titanium under tension were described in the study by Tan et al.[44] which includes the dominant basal slip and some prismatic slip in α-phase. Under loading, the basal slips cross the β-phase and then slip back

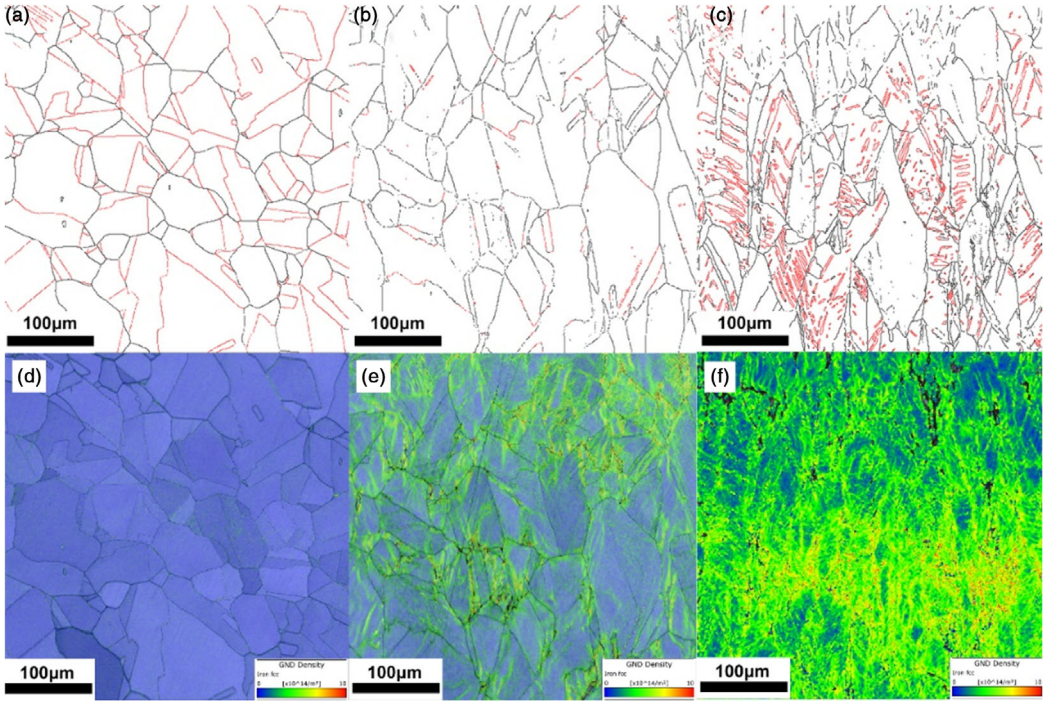

Figure 11. Electron backscatter diffraction for different deformation strain of a–c) twins and d–f) GND density in $Fe_{40}Mn_{40}Co_{10}Cr_{10}$ HEA. a) Initial sample with 57% twins, b) 12.7% twins at 40% strain, and c) 39.7% twins near fracture. d–f) GND 2D maps for initial, 40% strain and fracture of the sample; the color code legend is GND density values in ($\times 10^{14}$ m^{-2}).

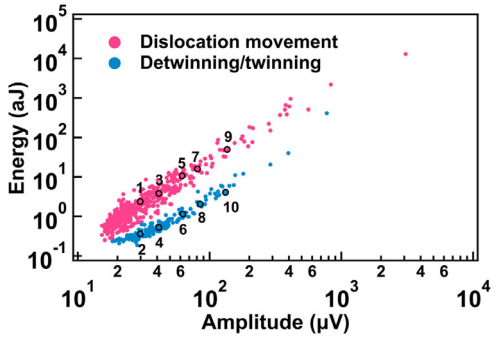

Figure 12. *E*(*A*) curve of dislocation movements (red) and detwinning/twinning (blue) in $Fe_{40}Mn_{40}Co_{10}Cr_{10}$ HEA with marked points for waveforms.

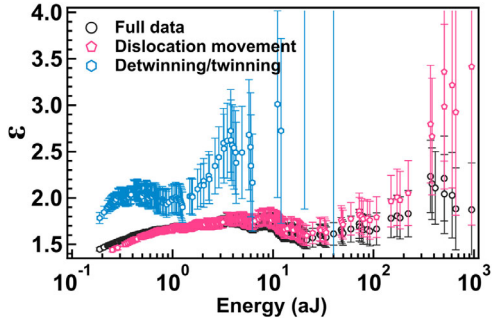

Figure 13. ML of dislocation movements (red), detwinning (blue), and full data (black) set in nickel.

into the α-phase. Our ex situ scanning electron microscope (SEM) observations (shown in **Figure 14**) indicate the same deformation mechanism. Tensile tests were stopped at a strain of 1%, 3%, 9%, and at the fracture point to observe the slip features during the deformation process. For deformation at 1% strain, the dislocation shows several basal slips in the α-phase and transgresses across

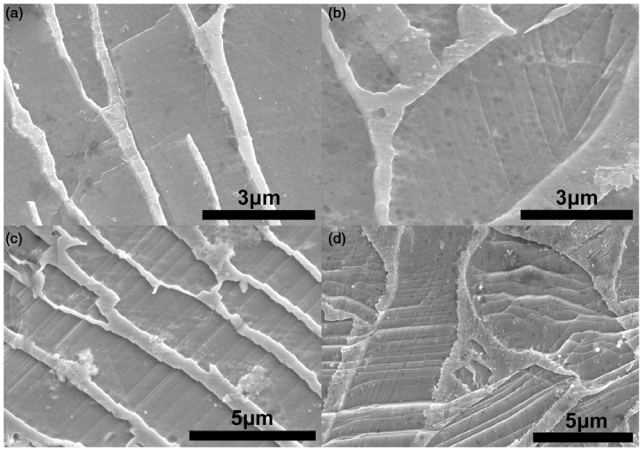

Figure 14. Dislocations in TC21. a) Several basal slips in the α-phase, which cross the β-phase with 1% deformation strain. b) Several basal slips in the α-phase transgress across the β-phase. Few prismatic slips occur at 3% deformation strain together with many basal slips. Slips crossing the phase boundaries occur during large deformation strain at c) ≈9% and d) near fracture.

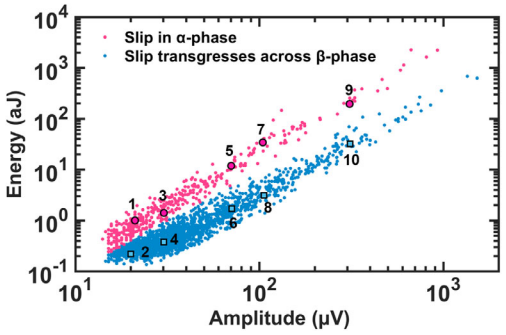

Figure 15. *E*(*A*) curve of basal slips in α-phase is represented in population 1 (red), and mixing of basal slip transmitting across β-phase and slipping back into α-phase is represented in population 2 (blue) with marked points for waveforms.

the β-phase (Figure 14a). When the sample is deformed by 3% strain, very few prismatic slips were generated (Figure 14b), except the basal slip in α/β-phase. Many basal slips and slip transmits occur for large deformation strains (Figure 14c-d).

The measured $E = S_i A_i^2$ scaling shows two populations. Their energy ratio S_1/S_2 is ≈4.8 (shown in **Figure 15**). The first population (red dots in Figure 15) with an exponent $\varepsilon = 1.6$ in ML (**Figure 16**) corresponds to the dislocation basal slips in the α-phase, in agreement with previous observations that the free dislocation movements show an avalanche exponent $\varepsilon = 1.6$.[42] The second population shown by blue dots relates to basal slips across the β-phase when slipping back into the α-phase, showing mixing behavior (Figure 16). Characteristic wave profiles of the two populations are shown in Figure S8, Supporting Information. The average durations of the two populations are different by a factor of 11.

4. Discussion

4.1. Possible Reasons for the Multiple Branches in $E-A^2$ Correlation

In "normal" scenarios, we see only a single-valued $E-A^2$ relationship[10,29] and virtually all previous work focused on this case. Here we have shown that an excellent fingerprint for the detection of coincidences between two mechanisms is the observation

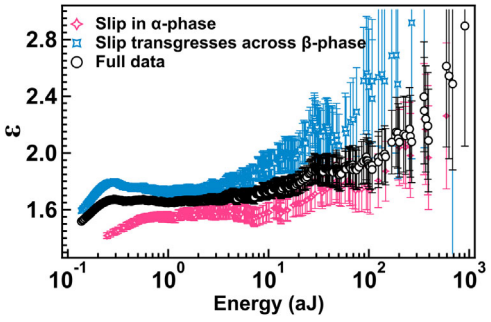

Figure 16. ML of basal slips in α-phase is represented in population 1 (red), and mixing of basal slip transmitting across β-phase and slipping back into α-phase is represented in population 2 (blue) with marked points for waveforms and full data set.

of a multivalued $E-A^2$ correlation, which we demonstrated in five different materials, for example, low-Ni 316L stainless steel, 316L stainless steel, polycrystalline Ni, TC21 titanium alloy, and $Fe_{40}Mn_{40}Co_{10}Cr_{10}$ high-entropy alloy. The fact that two branches in the $E-A^2$ relation appear in these materials was unexpected and reveals the potentially complex nature of superposed avalanche mechanisms. The question is then why do we observe multivalued $E-A^2$ correlations?

Theoretically, the energy of AE signals is defined as the integral over the squared amplitude $A(t)$, integrated over the duration of the avalanche $E \sim \int_0^D A(t)^2 dt$. If the lifetimes of individual AE signals are different for the two processes, the longer lifetimes shift the $E(A)$ correlations to higher energies. As for the present five materials, as shown in Figure 1, 6, 9, 12, and 15 and, all multivalued scaling in $E \sim A^2$ correlation shows that the branch for dislocation motion has higher energies in comparison with other deformation modes. This does not necessarily mean that each dislocation AE has a longer lifetime but that several AE signals can combine to generate longer AE sequences. The possible reasons are mainly attributed to dislocations that are easier to activate in comparison with other deformation mechanisms (such as twinning or martensitic transformation) and the accommodate deformation inside polycrystalline materials.

We first consider 316L stainless steel with the dislocation mode as an example. Two typical waveforms with similar maximum amplitudes around 200 μV are shown in **Figure 17**. From these profiles, we conclude that signals of an initial dislocation nucleation and growth decay roughly three times more slowly than entanglement avalanches. The average duration for all signals is 553 μs for dislocation movements and 188 μs for entanglements. Only one event determines the waveform of dislocation entanglements. This contrasts with the waveform of dislocation movements, which always contains multiple

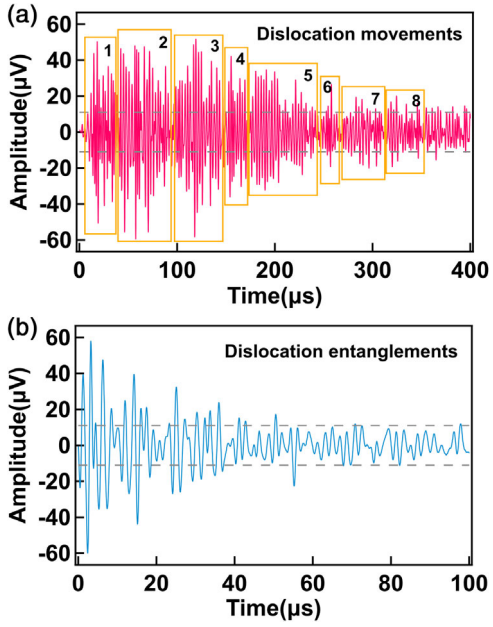

Figure 17. Acoustic waveform and frequency spectrum of a) dislocation movements and b) dislocation entanglements with maximum amplitudes near 60μV for 316L steel.

overlapping events. We conclude that the changes of the event durations reflect the accommodate deformation of the polycrystalline material and the movement of pre-existing dislocations. The plastic deformation in polycrystalline materials needs a concurrent activity of at least five independent slip systems, indicating that several dislocations need to be activated simultaneously or successively. In addition, the movement of pre-existing dislocations (Figure 5a) will further trigger the movements of other pre-existing dislocations. As a result, their avalanche profiles overlap, forming extremely long AE signals.

Second, for the cases of cold-rolled low-Ni 316L steel, polycrystalline Ni, and $Fe_{40}Mn_{40}Co_{10}Cr_{10}$ high-entropy alloy, multiple deformation modes are involved such as dislocation, twinning–detwinning, or martensitic transformation. The long AE signals for dislocation (Figure 17) not only contribute to the accommodation of polycrystalline deformation, but also indicate that dislocations are the easiest deformation modes among other possible deformation modes. It is known that for most FCC metals, the general stacking fault energy for the formation of full dislocation is lower than that of twinning, that is, dislocation movement is easier to activate than twinning under loading. For cold-rolled low-Ni 316L steel, the pre-existing dislocations further trigger the overlap of individual dislocation AE profiles.

Third, for the case of TC21, the easiest deformation mode relates to dislocation basal slips in the α-phase. The size of the α-phase is much greater than the β-phase; thus, the accommodate deformation of polycrystalline under loading generates long AE signals in the α-phase.

In summary, we present a very simple observation, which shows that avalanches relate to different mechanisms in five selected materials. The underlying reason is that one deformation mode is overlapped with several individual avalanche profiles, leading to long duration and high energies of AE signals.

Avalanches in polycrystalline sequences and single crystals are clearly distinguished in low-Ni 316L and sapphire. The typical duration of AE events due to twinning in low-Ni 316L steel is 80 μs (as shown in **Figure 18**c), which is in the same order as the reported typical duration of AE events due to twinning in sapphire (≈50 μs).[48] However, the duration of AE events due to dislocation reaches 1400 μs, which is much longer than the reported duration of dislocation in sapphire (19 μs).[48] The difference arises from the fact that the AE signals for dislocation movement stem not from one individual avalanche (as shown in Figure 17a), but it contains overlaps with several avalanches. In this article, we focused on the polycrystalline state, in which the accommodating deformation of the polycrystalline matrix is important. This contrasts with the work in the study by Tymiak et al.,[48] which focuses on single crystals, where only few specific slip systems can be activated under loading.

4.2. Potential Applications in Real-Time Monitoring

The analysis of AE events to distinguish between the sources of different origins is a long-standing issue. Various unsupervised and supervised machine learning algorithms for AE signals have been developed to identify the active source mechanism among other possible multiple sources[49–57]

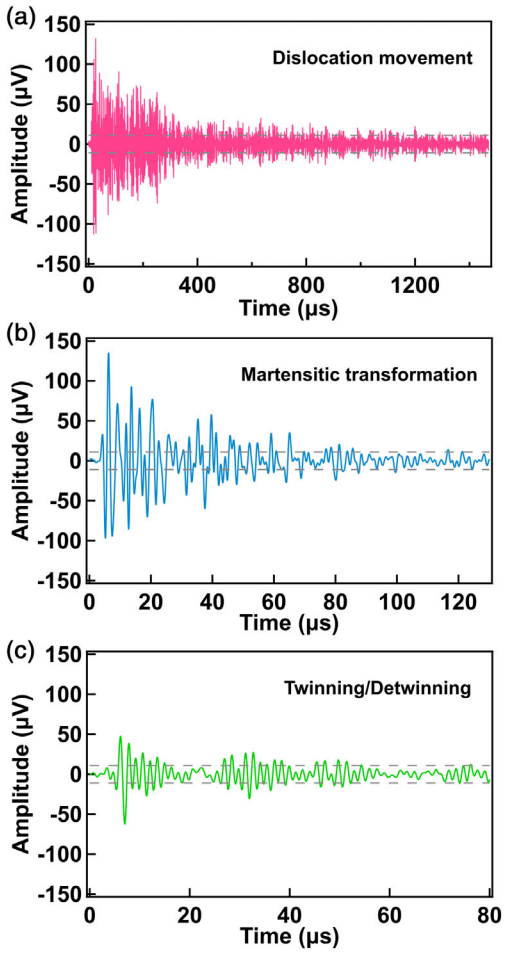

Figure 18. Typical profiles for a) dislocations and b) martensitic transformations with amplitudes around 150 μV, and c) typical profiles of detwinning/twinning. The material is low-Ni 316L steel.

Several unsupervised clustering techniques have been explored and found effective for a large variety of applications. *k*-means and fuzzy *c*-means schemes are among the best known and most widely used approaches.[55] The *k*-means algorithm finds spherical clusters and is therefore best suited for clustering convex data.[58] However, it remains unknown if AE data obey this constraint. In addition, *k*-means are iterative processes which hinder applications in real-time workflow.[55] To meet the requirements for AE real-time monitoring, noniterative, data-driven adaptive sequential *k*-means (ASK) were proposed.[55] Another viable alternative to *k*-means methods is the Gaussian mixture model (GMM).[59] In contrast to *k*-means, GMMs define Gaussian functions that model the input data and thus are well suited to clustering data sampled from Gaussian distributions. Moreover, they provide greater flexibility for the description of clustering. Although the above unsupervised machine learning algorithms do not require labeled data, and are intuitive and explainable, they are sensitive to the initialization, noise and outliers, and tend to fall into local minima.

Another clustering technique is the supervised machine learning, which required amounts of a priori information. For instance, such popular classifiers as neural networks or support vector machine have to be exposed to large-enough training sets representing all anticipating source mechanisms, which might be impossible or too expensive to obtain. It has been shown that the supervised machine learning algorithms can provide reasonable identification because the deformation mechanism during training can be identified by an in situ scanning electron microscope, ultrahigh-speed camera, or X-ray tomography.[50–54] However, the supervised machine learning algorithms meet a big challenge when multiple deformation mechanisms occur simultaneously on different spatial and temporal scales. This happens commonly in metals and alloys. On the one hand, the in situ observation techniques are insensitive to the evolution of local deformation. The label (or mechanism) for any AE signal during training is difficult to identify, and the problem is much greater when several mechanisms are superimposed. Historically, AE waveforms have been represented by parameters in the time domain (peak amplitude, voltage, energy, number of counts, duration, rise time, etc.), the frequency domain (average frequency, partial energy, etc), or by composite values comprising two or more basic values.[36,59–74] The majority of AE signals are nonstationary[75] which create strong correlations between the time domain and the frequency domain. In addition to this "parametric" description, both time and frequency analyses are needed to develop an accurate machine learning algorithm.[29,43]

Our statistical analysis allows to distinguish the coincident avalanche mechanisms with a clear physical understanding of their origins. Although the analysis is postmortem after the AE experiment is terminated, the obtained knowledge can help us to label the AE signals more accurately. At a later stage, AE real-time monitoring requires that a clustering algorithm assigns these mechanisms, while AE signals are being measured. For example, we envisage a supervised machine learning algorithm which considers the information of the time-frequency domain of AE signals under guidance of the statistical analysis. The machine learning algorithm can then potentially monitor dislocation movements, martensitic transformations, and detwinning /twinning in real-time.[43]

5. Conclusion and Perspectives

We demonstrated in this article that AE spectra contain much more information than traditionally expected. It encourages the practitioner to consider AE as a typical spectroscopic method, where applied fields, such as strain and electric fields, lead to local strain release. This strain release then propagates through samples via acoustic waves, which are detected by the AE equipment. The time evolution of the AE signals constitutes time-dependent spectra, the so-called jerk spectra. These jerk spectra contain a multitude of time correlations and fine structures which are often overlooked. In this article, we emphasize that it is possible to identify multiple mechanisms as the origin of AE spectra. Superposed AE species have been seen before using the first three approaches; the new approach based on the $E = S_i A_i^2$ scaling has not been reported before and allows a much more detailed analysis of the jerk spectra.

Multiple $E = S_i A_i^2$ scaling occurs in alloys because these alloys contain several mechanisms where local strain induces several

collapse mechanisms. Once the multiplicity of AE species is recognized, it becomes much easier to identify the subsets of data for the different avalanche mechanisms. It is then possible to identify the energy exponents (or amplitude exponents) for each subset and hence compare the dynamics of the various AE species. If, in contrast, the separation has not been achieved; one simply observes an average exponent, which has no obvious physical meaning.

This progress is crucial for the field of materials sciences and the analysis of fundamental physical processes. We have shown in this article that the mechanisms can be separated for some alloys. While there is a universal criterion for the failure threshold in slowly sheared BMGs[76], one cannot yet formulate a simple equation to describe an interaction and relate it to AE. Recent work implied some link between the multiple $E = S_i A_i^2$ scaling signals with the underlying mechanism,[45] more work on the universal material-dependent criterion for the multiple $E = S_i A_i^2$ scaling is urgently needed. In addition, similar scenarios are expected to exist more widely. One important field of applications relates to ferroic materials. The key question is the separation between AE signals due to domain switching, hole collapse, and dislocation movement. On an even finer scale, one wants to understand which domain movement is activated under which electric, magnetic, or elastic fields. The dynamic behavior of needle domains or sideways-moving domains is totally different, but it appears very likely that they will coincide in experiments.[8] The same problem exists for anisotropic movements. Fields in different orientations induce avalanches with a variety of exponents. However, despite these preliminary works, a systematic analysis of avalanches with mixed species in ferroics has not yet been undertaken but is urgently needed for electronic applications.

Supporting Information

Supporting Information is available from the Wiley Online Library or from the author.

Acknowledgements

Financial support from the Natural Science Foundation of China (51931004) and 111 project 2.0 (BP2018008) are gratefully acknowledged. E.K.H.S. is grateful to EPSRC (EP/P024904/1) and H2020 Marie Sklodowska-Curie Actions (861153).

Conflict of Interest

The authors declare no conflict of interest.

Keywords

acoustic emissions, avalanches, deformation mechanisms

Received: September 10, 2021
Revised: November 4, 2021
Published online:

[1] J. P. Sethna, K. Dahmen, S. Kartha, J. A. Krumhansl, B. W. Roberts, J. D. Shore, *Phys. Rev. Lett.* **1993**, *70*, 3347.
[2] M. J. Alava, P. Nukalaz, S. Zapperi, *Adv. Phys.* **2016**, *55*, 349.
[3] M. Zaiser, *Adv. Phys.* **2006**, *55*, 185.
[4] T. Richeton, J. Weiss, F. Louchet, *Nat. Mater.* **2005**, *4*, 465.
[5] E. K. Salje, K. A. Dahmen, *Annu. Rev. Condens. Matter Phys.* **2014**, *5*, 233.
[6] G. F. Nataf, P. O. Castillo-Villa, J. Baro, X. Illa, E. Vives, A. Planes, E. K. H. Salje, *Phys. Rev. E* **2014**, *90*, 022405.
[7] E. K. H. Salje, X. Wang, X. Ding, J. Sun, *Phys. Rev. B* **2014**, *90*, 064103.
[8] E. K. H. Salje, D. Xue, X. Ding, K. A. Dahmen, J. F. Scott, *Phys. Rev. Mater.* **2019**, *3*, 014415.
[9] E. Vives, J. Ortin, L. Manosa, I. Rafols, R. Perezmagrane, A. Planes, *Phys. Rev. Lett.* **1994**, *72*, 1694.
[10] Y. Chen, Q. B. Wang, X. D. Ding, J. Sun, E. K. H. Salje, *Appl. Phys. Lett.* **2020**, *116*, 111901.
[11] E. K. H. Salje, J. Koppensteiner, M. Reinecker, W. Schranz, A. Planes, *Appl. Phys. Lett.* **2009**, *95*, 231908.
[12] R. Niemann, J. Baro, O. Heczko, L. Schultz, S. Faehler, E. Vives, L. Manosa, A. Planes, *Phys. Rev. B* **2012**, *86*, 214101.
[13] F. J. Romero, J. Manchado, J. M. Martin-Olalla, M. C. Gallardo, E. K. H. Salje, *Appl. Phys. Lett.* **2011**, *99*, 011906.
[14] E. K. H. Salje, X. F. Wang, X. D. Ding, J. F. Scott, *Adv. Funct. Mater.* **2017**, *27*, 1700367.
[15] C. D. Tan, C. Flannigan, J. Gardner, F. D. Morrison, E. K. H. Salje, J. F. Scott, *Phys. Rev. Mater.* **2019**, *3*, 034402.
[16] M. C. Gallardo, J. Manchado, F. J. Romero, J. del Cerro, E. K. H. Salje, A. Planes, E. Vives, R. Romero, M. Stipcich, *Phys. Rev. B* **2010**, *81*, 174102.
[17] E. K. H. Salje, E. Dul'kin, M. Roth, *Appl. Phys. Lett.* **2015**, *106*, 152903.
[18] T. Vanorio, M. Prasad, A. Nur, *Geophys. J. Int.* **2003**, *155*, 319.
[19] T. Zou, J. Peng, M. Gottschalk, P. P. Zhang, Z. G. Mao, X. Ke, *Matter* **2019**, *31*, 195602.
[20] S. Liu, B. Phillabaum, E. W. Carlson, K. A. Dahmen, N. S. Vidhyadhiraja, M. M. Qazilbash, D. N. Basov, *Phys. Rev. Lett.* **2016**, *116*, 036401.
[21] A. Sharoni, J. G. Ramirez, I. K. Schuller, *Phys. Rev. Lett.* **2008**, *101*, 026404.
[22] J. Baro, A. Corral, X. Illa, A. Planes, E. K. H. Salje, W. Schranz, D. E. Soto-Parra, E. Vives, *Phys. Rev. Lett.* **2013**, *110*, 088702.
[23] E. Salje, *Phys. Chem. Miner.* **1985**, *12*, 93.
[24] E. K. H. Salje, *Annu. Rev. Mater. Res.* **2012**, *42*, 265.
[25] E. K. H. Salje, A. Planes, E. Vives, *Phys. Rev. E* **2017**, *96*, 042122.
[26] E. K. H. Salje, H. L. Liu, Y. Xiao, L. S. Jin, A. Planes, E. Vives, K. N. Xie, X. Jiang, *Phys. Rev. E* **2019**, *99*, 023002.
[27] H. Bauke, *Eur. Phys. J. B* **2007**, *58*, 167.
[28] A. Clauset, C. R. Shalizi, M. E. J. Newman, *SIAM Rev.* **2009**, *51*, 661.
[29] Y. Chen, X. D. Ding, D. Q. Fang, J. Sun, E. K. H. Salje, *Sci. Rep.* **2019**, *9*, 1330.
[30] E. K. H. Salje, H. L. Liu, L. S. Jin, D. Y. Jiang, Y. Xiao, X. Jiang, *Appl. Phys. Lett.* **2018**, *112*, 054101.
[31] D. Soto-Parra, X. X. Zhang, S. S. Cao, E. Vives, E. K. H. Salje, A. Planes, *Phys. Rev. E* **2015**, *91*, 060401.
[32] X. Jiang, H. L. Liu, I. G. Main, E. K. H. Salje, *Phys. Rev. E* **2017**, *96*, 023004.
[33] X. Jiang, D. Y. Jiang, J. Chen, E. K. H. Salje, *Am. Miner.* **2016**, *101*, 2751.
[34] J. J. Li, J. F. Fan, Z. Wang, Y. C. Wu, K. A. Dahmen, J. W. Qiao, *Intermetallics* **2020**, *116*, 106637.
[35] G. Wang, K. C. Chan, L. Xia, P. Yu, J. Shen, W. H. Wang, *Acta Mater.* **2009**, *57*, 6146.

[36] J. Antonaglia, W. J. Wright, X. J. Gu, R. R. Byer, T. C. Hufnagel, M. LeBlanc, J. T. Uhl, K. A. Dahmen, *Phys. Rev. Lett.* **2014**, *112*, 155501.
[37] B. A. Sun, H. B. Yu, W. Jiao, H. Y. Bai, D. Q. Zhao, W. H. Wang, *Phys. Rev. Lett.* **2010**, *105*, 035501.
[38] B. Casals, G. F. Nataf, D. Pesquera, E. K. H. Salje, *APL Mater.* **2020**, *8*, 011105.
[39] B. Casals, G. F. Nataf, E. K. H. Salje, *Nat. Commun.* **2021**, *12*, 345.
[40] J. J. Li, J. W. Qiao, Y. C. Wu, *J. Alloys Compd.* **2020**, *819*, 152941.
[41] Y. Zhang, J. P. Liu, S. Y. Chen, X. Xie, P. K. Liaw, K. A. Dahmen, J. W. Qiao, Y. L. Wang, *Prog. Mater. Sci.* **2010**, *90*, 358.
[42] Y. Chen, B. Go, X. Ding, J. Sun, E. K. Salje, *J. Mater. Sci. Technol.* **2021**, *92*, 31.
[43] Y. Chen, B. Gou, W. Fu, C. Chen, X. Ding, J. Sun, E. K. Salje, *Appl. Phys. Lett.* **2020**, *117*, 262901.
[44] C. Tan, Q. Sun, L. Xiao, Y. Zhao, J. Sun, *J. Alloys Compd.* **2017**, *724*, 112.
[45] B. Casals, K. A. Dahmen, B. Y. Gou, S. Rooke, E. K. H. Salje, *Sci. Rep.* **2021**, *11*, 5590.
[46] D. M. Dimiduk, M. D. Uchic, T. A. Parthasarathy, *Acta Mater.* **2005**, *53*, 4065.
[47] A. M. Hussein, S. I. Rao, M. D. Uchic, D. M. Dimiduk, J. A. El-Awady, *Acta Mater.* **2015**, *85*, 180.
[48] N. I. Tymiak, A. Daugela, T. J. Wyrobek, O. L. Warren, *Acta Mater.* **2004**, *52*, 553.
[49] P. Zhang, Y. Yang, Z. Huang, J. Sun, Z. Liao, J. Wang, Y. Yang, *Chem. Eng. Sci.* **2021**, *229*, 116083.
[50] H. Liu, S. Liu, Z. Liu, N. Mrad, A. S. Milani, *IEEE Trans. Ind. Electron.* **2021**, *68*, 2532.
[51] T. Shiraiwa, K. Tamura, M. Enoki, *Mater. Sci. Eng. A* **2017**, *768*, 11.
[52] M. L. Linderov, C. Segel, A. Weidner, H. Biermann, A. Y. Vinogradov, *Phys. Metals Metallogr.* **2018**, *119*, 388.
[53] A. Vinogradov, E. Vasilev, M. Linderov, D. Merson, *Mater. Sci. Eng. A* **2016**, *676*, 351.
[54] C. Van Steen, L. Pahlavan, M. Wevers, E. Verstrynge, *Constr. Build. Mater.* **2019**, *197*, 21.
[55] E. Pomponi, A. Vinogradov, *Mech. Syst. Signal Process.* **2013**, *40*, 791.
[56] H. A. Sawan, M. E. Walter, B. Marquette, *Compos. Sci. Technol.* **2015**, *107*, 89.
[57] J. P. McCrory, S. K. Al-Jumaili, D. Crivelli, M. R. Pearson, M. J. Eaton, C. A. Featherston, M. Guagliano, K. M. Holford, R. Pullin, *Composites B-Eng.* **2015**, *68*, 424.
[58] A. K. Jain, *Pattern Recognit. Lett.* **2010**, *31*, 651.
[59] A. K. Das, D. Suthar, C. K. Y. Leung, *Cem. Concr. Res.* **2019**, *121*, 42.
[60] W. Alchakra, K. Allaf, J. M. Ville, *Appl. Acoust.* **1997**, *52*, 53.
[61] R. K. Elsley, L. J. Graham, *Pattern Recognit. Acoust. Imag.* **1987**, *0768*, 285.
[62] M. Johnson, *NDT&E Int.* **2002**, *35*, 367.
[63] V. Kostopoulos, T. H. Loutas, A. Kontsos, G. Sotiriadis, Y. Z. Pappas, *NDT&E Int.* **2003**, *36*, 571.
[64] R. de Oliveira, A. T. Marques, *Comput. Struct.* **2008**, *86*, 367.
[65] M. Moevus, N. Godin, M. R'Mih, D. Rouby, P. Reynaud, G. Fantozzi, G. Farizy, *Compos. Sci. Technol.* **2008**, *68*, 1258.
[66] R. Gutkin, C. J. Green, S. Vangrattanachai, S. T. Pinho, P. Robinson, P. T. Curtis, *Mech. Syst. Signal Proc.* **2011**, *25*, 1393.
[67] S. Momon, N. Godin, P. Reynaud, M. R'Mili, G. Fantozzi, *Composites A* **2012**, *43*, 254.
[68] M. G. R. Sause, A. Gribov, A. R. Unwin, S. Horn, *Pattern Recognit. Lett.* **2012**, *33*, 17.
[69] E. Maillet, G. N. Morscher, *Mech. Syst. Signal Process.* **2015**, *52–53*, 217.
[70] L. Li, Y. Swolfs, I. Straumit, X. Yan, S. V. Lomov, *J. Compos Mater.* **2016**, *50*, 1921.
[71] J. Capek, M. Knapek, P. Minarik, J. Dittrich, K. Mathis, *Metals* **2018**, *8*, 644.
[72] V. Tra, J. Y. Kim, I. Jeong, J. M. Kim, *Sustainability* **2020**, *12*, 6724.
[73] K. Mathis, F. Chmelik, M. Janecek, B. Hadzima, Z. Trojanova, P. Lukac, *Acta Mater.* **2006**, *54*, 5361.
[74] M. A. Lebyodkin, I. V. Shashkov, T. A. Lebedkina, K. Mathis, P. Dobron, F. Chmelik, *Phys. Rev. E* **2013**, *88*, 042402.
[75] N. E. Huang, Z. Shen, S. R. Long, M. L. C. Wu, H. H. Shih, Q. N. Zheng, N. C. Yen, C. C. Tung, H. H. Liu, *Proc. R. Soc. A* **1971**, *454*, 903.
[76] Y. S. Luo, Z. Wang, J. Eckert, J. W. Qiao, *J. Appl. Phys.* **2021**, *129*, 155109.

Yan Chen completed her PhD in material science and engineering at Xi'an Jiaotong University in 2021. She came to Cambridge for a short visit from 2019 to 2020. Her main research is about identification and monitoring of different deformation mechanisms in metal and alloys based on acoustic emission and machine learning.

Xiangdong Ding completed his PhD at Jilin University of Technology in 1999 and became Professor at Xi'an Jiaotong University in 2008. His major interest is the phase transformation and mechanical behaviour of materials by using multiscale simulation methods and experiments. He has published over 200 scientific papers.

Ekhard Salje completed his PhD at Leibnitz University Hanover in 1972 and became Professor and head of department in Hanover in 1983. In 1985 he moved to Cambridge where he became professor of Mineral Physics and, later, Mineralogy and Petrology. He was Head of the Department of Earth Sciences and published over 700 scientific papers. He was elected Fellow of the Royal Society, and other national and international academies of science. He holds an honorary PhD, the Order of Merit (Germany) and is chevalier dans l'ordre des palmes academique (France).